RSC Publishing Faraday Discussions

Multiple pulse coherent dynamics and wave packet control of the N_2 a" $^1\Sigma_g^+$ dark state by attosecond four wave mixing

Journal:	*Faraday Discussions*
Manuscript ID	FD-ART-04-2018-000074.R1
Article Type:	Paper
Date Submitted by the Author:	02-May-2018

Complete List of Authors:	Warrick, Erika; E O Lawrence Berkeley National Laboratory, Chemical Sciences; University of California, Dept of Chemistry Fidler, Ashley; E O Lawrence Berkeley National Laboratory, Chemical Sciences; University of California, Dept of Chemistry Cao, Wei; E O Lawrence Berkeley National Laboratory, Chemical Sciences; University of California, Dept of Chemistry Bloch, Etienne; E O Lawrence Berkeley National Laboratory, Chemical Sciences Neumark, Daniel; University of California, Dept of Chemistry Leone, Stephen; University of California, Dept of Chemistry; University of California, Dept of Physics

Faraday Discussions

Paper

Multiple pulse coherent dynamics and wave packet control of the N_2 a″ $^1\Sigma_g^+$ dark state by attosecond four wave mixing

Received 00th January 20xx,
Accepted 00th January 20xx

DOI: 10.1039/x0xx00000x

www.rsc.org/

Erika R. Warrick, [a,b] Ashley P. Fidler, [a,b] Wei Cao, [a,b] Etienne Bloch, [a] Daniel M. Neumark [a,b] and Stephen R. Leone [a,b,c]

Nonlinear multidimensional spectroscopy is ubiquitous in the optical and radio-frequency regimes as a powerful tool to access structure and dynamics. The extension of this technique into the extreme ultraviolet (XUV) with attosecond pulses holds the promise of probing electronic dynamics and correlations with unprecedented time and spatial resolution. In this work, we use noncollinear four-wave mixing of a weak XUV attosecond pulse train (11-17 eV) and few-femtosecond NIR pulses (800 nm) to spectroscopically and dynamically probe the dipole-forbidden double-well potential of the a″ $^1\Sigma_g^+$ electronic state of nitrogen. The results demonstrate optical coupling of the inner and outer limits of the initially XUV-prepared vibrational wave packet in the valence character b' $^1\Sigma_u^+$ state to the inner and outer wells, respectively, of the a″ $^1\Sigma_g^+$ double well state by 800 nm light. Two four-wave mixing schemes with different pulse timing sequences and noncollinear beam geometries are used (one NIR pulse collinear and one NIR pulse noncollinear versus both NIR pulses noncollinear to the XUV) to measure the a″ dark state energetic structure and to control the dynamical preparation and motion of a dark state wave packet by selective population of either the inner Rydberg or outer valence-character potential well. Experimental measurements of the a″ $^1\Sigma_g^+$ outer well vibrational spacing and anharmonicity closely match the values theoretically predicted for this previously unobserved state.

1 Introduction

In small molecular targets, such as nitrogen, electronic excitation by broadband coherent light in the extreme ultraviolet (XUV) leads to a superposition of electronically excited states. The resulting multi-eV-spanning wave packet includes vibrational and rotational motion, and the coherent dynamics evolve on a sub-femtosecond timescale corresponding to the energy spacing of the levels that make up the wave packet. The typically very dense absorption spectra of small

[a] Chemical Sciences Division, Lawrence Berkeley National Laboratory, Berkeley, California 94720, USA.
[b] Department of Chemistry, University of California, Berkeley, California 94720, USA.
[c] Department of Physics, University of California, Berkeley, California 94720, USA.

molecules in this spectral region, with numerous overlapping vibronic transitions, can make it difficult to investigate the ultrafast motion that results from these correlated electronic and nuclear degrees of freedom using standard absorption techniques. In the visible region of the electromagnetic spectrum, nonlinear wave-mixing spectroscopy with femtosecond laser pulses has been successfully applied to disentangle complex spectra,[1] enabling the investigation of dynamics resulting from electronic,[2] vibrational,[3] and vibronic[4] coupling in complicated molecular, solvent environment, and solid-state systems. These multidimensional spectroscopies, including photon echos,[5] coherent anti-Stokes Raman scattering,[6] transient grating,[7] and two-dimensional optical and infrared spectroscopy,[8] use pulse sequences and interaction geometries to isolate particular time-dependent signals of interest. In addition, the selection rules that govern nonlinear experiments differ from those of linear processes, which allows for the study of molecular states that interact weakly, or are forbidden, under usual absorption conditions.[9] The extension of these wave-mixing techniques into the XUV spectral range permits the probing of core and valence electronic excitations with unprecedented time resolution.[10]

Limited by the low flux of high harmonic XUV light sources, recent work in this area has explored the combination of an attosecond XUV light source with a few-femtosecond near-infrared (NIR) pulse.[11] In molecular targets, such as nitrogen, these non-degenerate photon energies allow for the selective probing of vibrational motion in highly excited electronic states. Wave-mixing in a collinear beam geometry, known as attosecond transient absorption spectroscopy, results in a multitude of coupled electronic and nuclear motions in molecules that require extensive theoretical effort to interpret.[12–15] However, it has recently been shown that crossing the NIR and XUV beams at a small angle in the sample creates an additional spatial dimension for signal detection based on wave vector phase matching.[16,17] In this geometry, signals resulting from different NIR-induced coupling pathways and wave mixing orders that generate light at the same energy can be disentangled based on their detection angle. This allows the selection of particular signals of interest and their detection free from other competing effects.

Previous wave-mixing experiments in nitrogen focused on understanding the NIR driven coupling of electronic and vibrational levels excited by the XUV pulse.[12,14] Under the influence of the NIR field, energy was exchanged between electronic and vibrational energy levels.[12] Theoretical simulations highlighted the importance of dark state levels of the nitrogen molecules in mediating these processes, but these states could not be directly accessed or characterized experimentally at the time.[14] The direct characterization of dark state levels in XUV-NIR wave mixing experiments in atomic systems has recently been demonstrated. For example, the addition of a NIR pulse coaxial and time-coincident with the XUV pulse in a collinear geometry was used to create a coherent superposition of bright and dark states of atomic neon.[18] A time-delayed NIR pulse was able to couple these levels, resulting in time-dependent interference features with periods corresponding to the energy separation between NIR-coupled bright and dark states. When a similar pulse sequence was implemented in a noncollinear wave mixing geometry in another atomic system, argon, the wave packet created in the dark states could be probed directly via spatially isolated emission features (angle-resolved wave vector phase matching).[16] The observed quantum beats in the emission features correspond directly to the dark state energy level spacing. In this paper, these noncollinear techniques are applied to a complex set of electronic states of molecular nitrogen to directly probe the dark states implicated in the dynamics observed

in previous collinear wave-mixing experiments. Both spectral and time-resolved measurements are used to reveal the key dynamics.

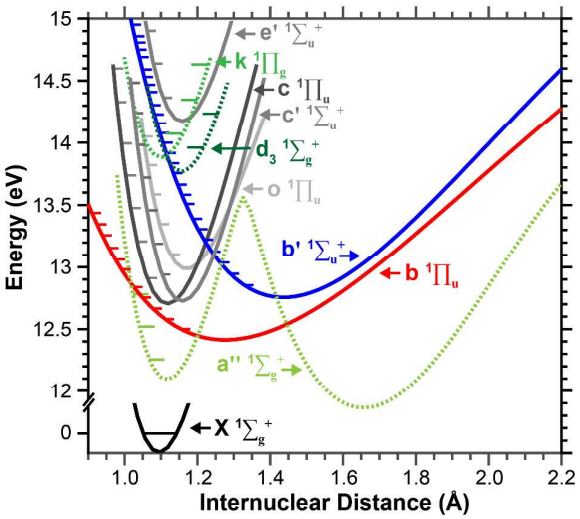

Figure 1: Schematic of relevant nitrogen potential energy curves. Optically allowed states are shown with solid lines. Optically forbidden, dark, states are presented as green dashed curves.

Overview of Nitrogen Electronic State Spectroscopy

The optically allowed, bright, states of nitrogen in the 12-15 eV range have been the subject of numerous linear absorption studies. The complicated absorption spectrum in this energy range was satisfactorily assigned to five different electronic states only after high resolution synchrotron spectroscopic studies became possible and with the development of configuration interaction theory in 1969.[19–21] With these advances, the transitions below the first ionization threshold of nitrogen at 15.5808 eV[22] were assigned to both Rydberg and non-Rydberg electronic states. A schematic of the relevant states is presented in Figure 1. There are two Rydberg series comprising of an *np* electron bound to the ground state ionic core, X $^2\Sigma_g^+$. The lowest members of these two series are c $^1\Pi_u$, formed by excitation to the 3pπ orbital, and c′ $^1\Sigma_u^+$, formed by population of the 4pσ orbital. Higher members of these series up to n= 39 have also been assigned,[23] with the labels e and e′ being assigned to the next (n=4) members of each series. There is also a Rydberg series built on the A $^2\Pi_u$ excited state ion, known as o, which is formed by the excitation of an electron to the 3sσ_g Rydberg orbital. Finally, there are also transitions to two non-Rydberg states in this energy range. These valence states are formed by excitation to molecular orbitals that are less diffuse than those of the Rydberg states. As a result, these states have weaker chemical bonds with longer equilibrium bond lengths and significantly altered vibrational structure compared to the Rydberg states. The b $^1\Pi_u$ valence state is the lowest dipole allowed state accessible in nitrogen, with the v = 0 level at 12.5 eV, while the b′ $^1\Sigma_u^+$ state is accessed at energies between 13.5 and 14.5 eV. The coherent electronic and vibrational dynamics in these bright states induced by an attosecond XUV pulse were probed using a time-delayed few-femtosecond NIR pulse, as in previous experiments.[12,14]

The states of *gerade* symmetry in nitrogen, which are optically forbidden from the ground state, are less well known because of the difficulty implicit in accessing them. There are predicted to be dark states of both Rydberg and valence character, similar to the electronic bright

states of nitrogen. Slightly more is known about dark states of Rydberg character due to their favorable Franck-Condon overlap with the ground state of nitrogen, which allows for their excitation through multiphoton transitions.[24–26] The lowest lying Rydberg character dark state consists of a 3sσ electron bound to the lowest ionic core of nitrogen to form a state of $^1\Sigma_g^+$ symmetry. The most accurate molecular constants for this state, the a″ $^1\sum_g^+$state, were measured using ionization with a third photon in 2+1 Resonance Enhanced Multiphoton Ionization (REMPI) experiments. These constants include a term energy T_0 of 12.25467 eV[25] and molecular constants ω_e= 0.27103 eV and $\omega_e x_e$ = 2.6 meV.[24] Higher energy Rydberg character dark states have also been identified using multiphoton excitation at energies above 14 eV.[27,28] These include the k $4d\pi_g$ state[27] and the d_3 $3d\sigma_g$ state,[29,30] which are Rydberg states built on the X N_2^+ ion core.

Substantially less is known about the dark states of valence character in this energy region in nitrogen. Ab initio calculations using configuration interaction[31–37] and R-matrix methods[29] to model non-Rydberg states of N_2 find that the lowest state of $^1\Sigma_g^+$ symmetry is a valence state that is strongly bound with a dissociation energy of more than 3 eV.[35] The calculated molecular constants for this state place the bottom of the well at 11.02 eV, predict a substantially elongated equilibrium bond length of 1.576 A, and suggest closely spaced anharmonic vibrational energy levels with molecular constants of ω_e = 0.116 eV and $\omega_e x_e$ = 0.37 meV.[37] The dominant electronic configuration of this state, 80%, is predicted to be the doubly excited $(2p_{x/y}\pi_u)^2(2p_z\sigma_g)^2(2p_{x/y}\pi_g)^2$ configuration, while the minor contribution, mainly at larger separations, is from the $(2p_{x/y}\pi_u)^3(2p_z\sigma_g)(2p_{x/y}\pi_g)(2p_z\sigma_u)$ configuration. Due to their identical symmetries, this state is posited to have an avoided crossing with the a″ Rydberg state discussed above, resulting in only one or two bound vibrational levels in the Rydberg state well.[31,32] This avoided crossing will lead to a double well potential for this dark state, with the inner well corresponding to the a″ $^1\Sigma_g^+$ Rydberg state and the outer well to the $^1\Sigma_g^+$ valence state. Experimental observations of this theoretically proposed outer well valence state have so far been limited to two tentative assignments of fragmentary rotational structure that perturbs the observed bright state REMPI transitions.[38,39] Direct observation and better characterization of this state is of particular interest for atmospheric modeling, since it has been hypothesized to play a critical role as an intermediate state in the predissociation of higher energy bright and dark Rydberg states.[40,41]

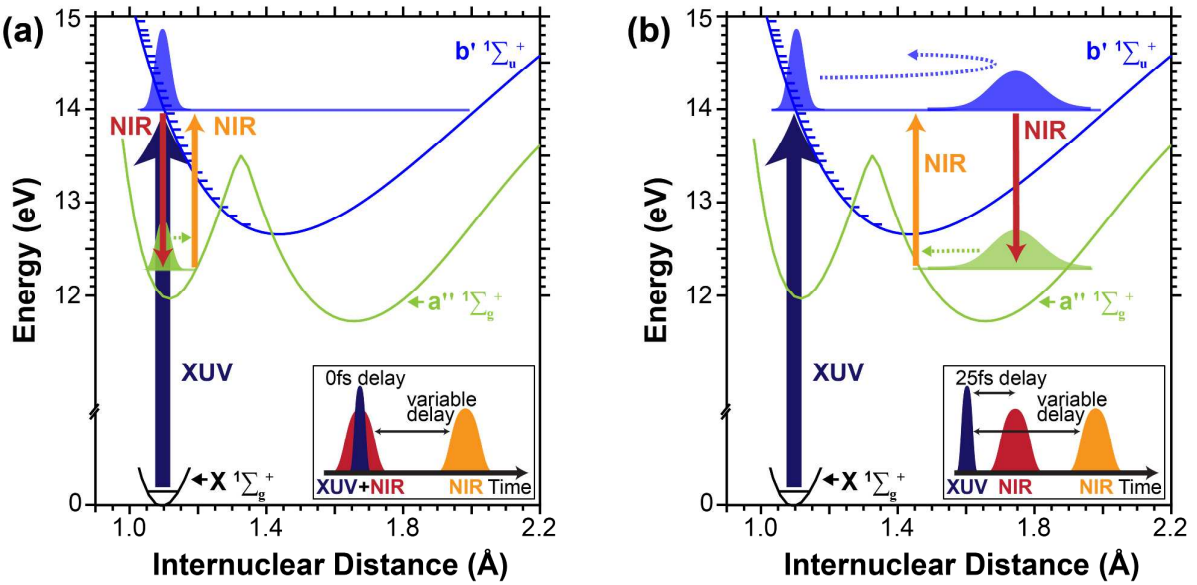

Figure 2: Schematic of wave-mixing experiment in nitrogen. Only the bright valence b′ $^1\Sigma_u^+$ state and double-well dark a″ $^1\Sigma_g^+$ states are shown for simplicity. (a) and (b) illustrate the dark state wave packet that can be generated in the inner and outer wells of the a″ $^1\Sigma_g^+$ state, respectively. The insets show pulse sequences that are used in a coherent control experiment to selectively generate these specific dark state wave packets.

Overview of Nitrogen Coherent State Dynamics

Figure 2 summarizes the principle of the wave-mixing process that is used to directly probe the double well a″ dark state in this experiment. An XUV pulse produced using high harmonic generation populates multiple electronic states, including the b′ valence state. The vibronic wave packet that is formed in this state freely evolves from its original preparation in the Franck-Condon region to longer internuclear distances. A first NIR pulse projects this wave packet onto the vibrational levels of the two-photon allowed a″ state. A second NIR pulse, with a variable delay relative to the (XUV+NIR) pulse pair and a fixed angle relative to these two beams, drives transitions back to the bright state vibrational levels in the b′ state. The nonlinear polarization that results from these three-photon interactions radiates XUV light as the four-wave mixing signal. Using a noncollinear beam interaction geometry, where one or both NIR beams are angled relative to the XUV beam, allows for the spatial isolation of this four-wave mixing signal through angle-resolved wave vector phase matching. By varying the time delay of the second NIR pulse and monitoring the time-resolved XUV emission of individual final state levels with spectrally and spatially resolved detection, wave packet dynamics in the dark state potential wells are probed with excellent time resolution and spectroscopic accuracy. This is in contrast to previous experiments, where a single time-delayed NIR pulse only allowed access to bright state dynamics.[12,14]

In this paper, two different experimental configurations are used to probe the dark states of nitrogen. Spectroscopic characterization of electronic dark states is achieved in a noncollinear experiment (one NIR beam collinear and one NIR beam noncollinear) where a first collinear and time coincident XUV-NIR pulse interaction spanning 10s of femtoseconds is used to generate two photon excitation to the gerade states of nitrogen, including the a″ $^1\Sigma_g^+$ state. A noncollinear NIR pulse is then used to probe this dark state wave packet at variable time delays. The resultant quantum beats oscillate with periods corresponding to the dark state vibrational spacing. The

0.107 eV fundamental vibrational frequency of the theoretically predicted a″ $^1\Sigma_g^+$ outer well is experimentally measured for the first time using this technique. The broadband pulses used in this experiment and the multilevel detection scheme allow for experimental observation of the anharmonicity of this well through the detection of overtone transitions and the shift of the fundamental frequency. In addition, emission due to dark states of Rydberg character including the a″ $^1\Sigma_g^+$ inner well and higher energy k and d_3 states are also observed. In a second noncollinear experiment using an interaction geometry where both NIR beams are noncollinear to the XUV beam, wave packet control is demonstrated in the simplified target state picture (Figure 2) using two independently delayed few-femtosecond NIR pulses. The delay between the XUV and first NIR pulse is used to selectively create a wave packet in either the inner or outer potential well of the a″ $^1\Sigma_g^+$ state. This preparation is confirmed by the observation of characteristic dark state quantum beats in emission following the action of the scanned second NIR pulse. These two experiments demonstrate how tabletop multidimensional spectroscopy with attosecond XUV pulses can be used to study dynamics associated with valence electronic excitations in a simple molecular system.

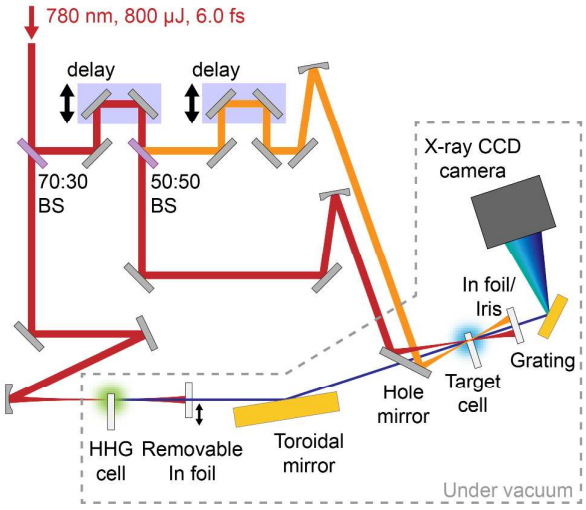

Figure 3: Experimental apparatus for all beam noncollinear experiments. BS = Beamsplitter, In = Indium. For experiments using a collinear NIR beam, the indium foil after the HHG cell is removed, allowing the generating NIR arm to propagate collinearly and overlapped in time with the XUV pulse. Only one of the variably delayed NIR arms is used in this geometry.

2. Experimental Methods

The experimental apparatus used in these experiments is schematically presented in Figure 3. The 22 fs output of a commercial 2 mJ, 1 kHz titanium-sapphire laser system (Femtopower HE, Femtolasers) is spectrally broadened in a neon-filled hollow core fiber. Six pairs of chirped mirrors (Ultrafast Innovations) are used to compress the resulting pulses to durations of 5 fs, with spectral bandwidth spanning 550 nm to 950 nm. A 70:30 beamsplitter directs the majority of the power to a 1.5 mm diameter cell statically filled with xenon, where high harmonic generation is used to produce an attosecond pulse train in the XUV. The electric field of the NIR light is modified using two quartz plates and a BBO crystal in a double optical gating configuration[42] to generate a continuous spectrum of XUV light. A 100 nm indium foil blocks the residual NIR

light and limits the XUV bandwidth to 11-17 eV. Experiments utilizing a copropagating NIR pulse are performed by removing this filter.

The smaller fraction of NIR light is delayed relative to the XUV arm using a piezoelectric stage. It is recombined noncollinearly by vertically displacing the beam upward from the 3 mm hole of a 1 inch diameter annular mirror that the XUV passes through. The crossing angle of the two beams in the interaction region is deduced from the interference fringes between the NIR pulse used for harmonic generation and the delayed NIR pulse. The angle of the upper NIR beam and the XUV beam is measured to be 18 mrad or 1º. For experiments using two independently delayed NIR pulses, an additional 50:50 beamsplitter is used to split this NIR beam. A second piezoelectric stage introduces an additional delay, and the beam is directed to a position on the hole mirror that is vertically displaced downwards from the hole. The interference pattern between this lower beam and the NIR pulse used for harmonic generation (i.e. the path of the XUV beam) measures a 13 mrad interaction angle.

After the interaction region, the noncollinear NIR light is blocked using an iris. A 150 nm indium foil performs this function in experiments with a collinear NIR beam. The spectrum of the XUV light is recorded using a spectrometer consisting of a flat-field grating (01-0464, Hitachi) and an x-ray CCD camera (Pixis XO 400B, Princeton Instruments). Using a measurement of argon absorption lines, the spectral resolution was determined to be 19 meV at 14.3 eV.

For these experiments, the 3 mm length target cell was filled with 10 Torr of nitrogen gas. Each delay point is the average of 3 images accumulated for 1500 laser pulses. A delay step size of 1 fs was used to keep acquisition times reasonable while resolving dynamics on timescales of few to hundreds of femtoseconds. The images were calibrated in energy using known transitions of argon and in angle using measured propagation distances. Camera image data are presented as raw XUV flux to highlight the magnitude of the emission features. Time-dependent spectra are shown as absorption, $A = -\log_{10}(I_{trans}/I_{ref})$, where the light generated with sample present is divided by a reference spectrum with no sample present taken at the beginning of the scan. Emission features have negative absorption values. This presentation emphasizes small changes in the strength of the emission features in the time-delay dependent spectra, which allows for the comparison of time-dependent behavior at different camera angles.

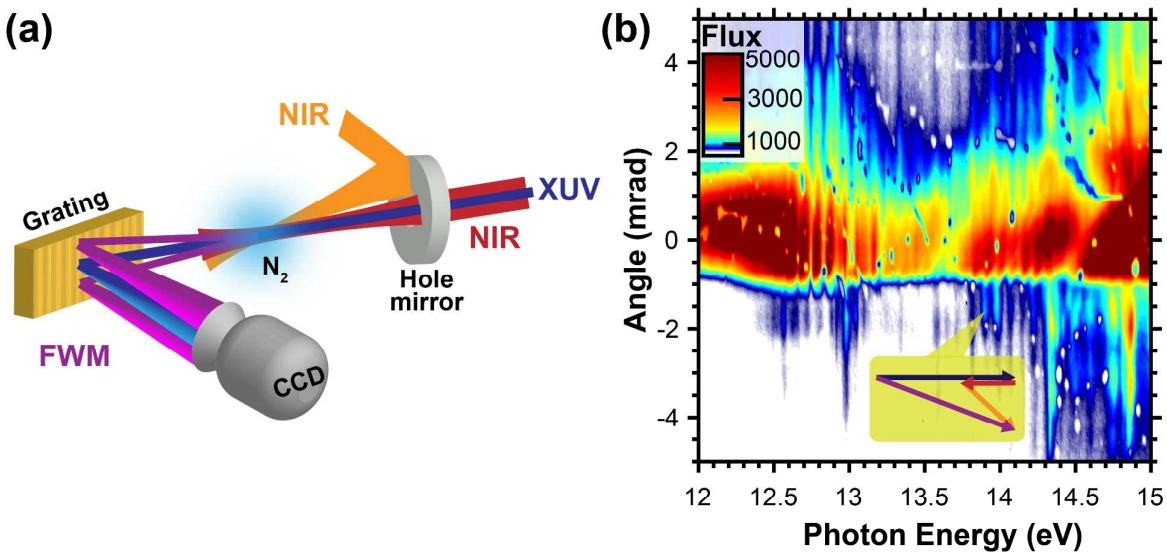

Figure 4: (a) Noncollinear beam geometry. (b) Camera image at overlap of (XUV+NIR) and noncollinear NIR beams presented in XUV photon flux.

3. Dark State Spectroscopic Characterization Using Collinear NIR+XUV and a Noncollinear NIR Beam

The dark states of molecular nitrogen are inaccessible in traditional static absorption spectroscopy. A wave mixing experiment was designed to probe these states directly using two photons to excite an initial wave packet composed of both bright and dark electronic states. For this experiment, the 100 nm indium foil after the harmonic cell is removed, which allows the driving NIR pulse to copropagate with the generated XUV pulse. These two pulses are spatiotemporally overlapped and propagate collinearly through the nitrogen target. The pulse duration of the copropagating NIR pulse is lengthened due to the high harmonic generation process. As a result, this XUV-NIR pulse pair can access dark states both within and outside of the Franck-Condon region. A second, time-delayed, few-femtosecond NIR pulse crosses these beams at a small angle at the target in order to probe the dark state wave packet dynamics by generating four wave mixing signals that are spatially isolated from the transmitted XUV beam. This experimental wave-mixing configuration is illustrated in Figure 4.

The camera image with all three pulses arriving simultaneously is presented as XUV flux in Figure 4(b). The transmitted XUV beam has a broad spectrum spanning 12 to 17 eV, and it has a relatively narrow divergence between -1 and 2 mrad, where this angle is defined as shown in Figure 4(b). Negative divergence angles correspond to features below the incident harmonic-generated XUV light on the camera, while positive are above. The XUV spectrum is strongly modulated by absorption features corresponding to the bright states of nitrogen between 12.5 and 15 eV. Narrow emission features are observed displaced vertically both above and below the harmonic spectrum at energy positions that also correspond to these bright states. Based on energy conservation and momentum conservation (wave vector phase matching) considerations, these emission signals correspond to specific nonlinear dipole responses following the wave vector matching equation $k_{FWM} = k_{XUV} \pm k_{NIR1} \pm k_{NIR2}$. Emission features between 13.5 eV

and 14.5 eV with emission angles of -1 mrad to -2.5 mrad can be assigned to a wave mixing process involving both NIR pulses. For the emission features found below the harmonic axis, the emission occurs as a result of the polarization dipole formed between the b′ vibrational states around 14 eV and the ground state of nitrogen. This coherence is induced by a four-wave-mixing process where the combined action of the XUV pulse and copropagating NIR pulse coherently populates vibrational levels in the a″ dark state around 12.25 eV, and then the noncollinear NIR beam transfers part of the population of these states to the same final b′ state around 14 eV. The involved potential energy curves are shown in Figure 2. The spatial position of the emission features below the harmonic axis is determined by the crossing angle of the NIR pulse with the collinear XUV and NIR beam, as is shown in the wave mixing diagram inset in Figure 4(b). With a measured crossing angle of α=18 mrad for the NIR beam, features arising from such a process should appear at $\theta \approx \alpha * \frac{-1.75}{14}$ =-2.25 mrad, consistent with the experimental observation of -2.06 mrad.

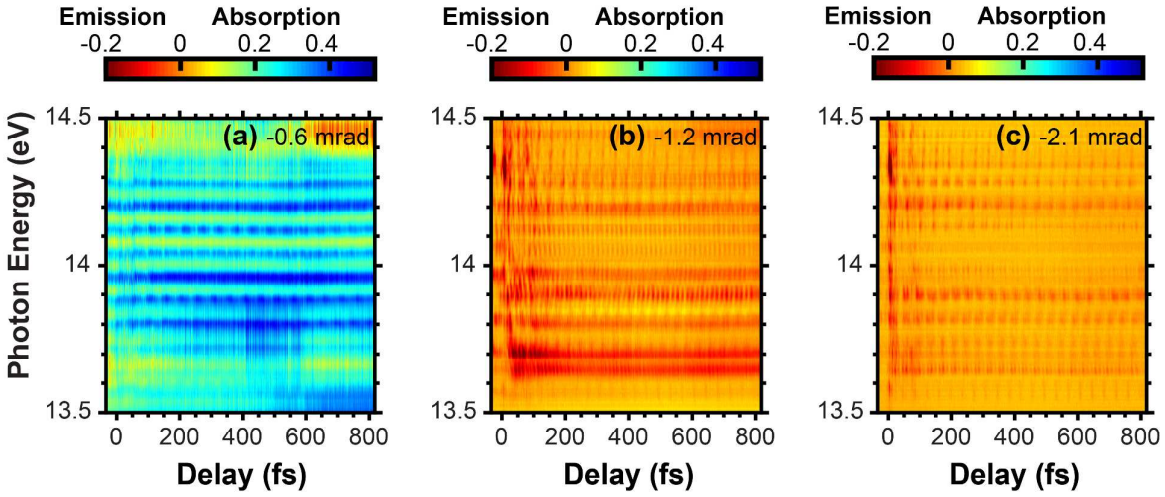

Figure 5: Time dependence of absorption and emission features at different camera divergence angles collected in the noncollinear geometry shown in Figure 4.

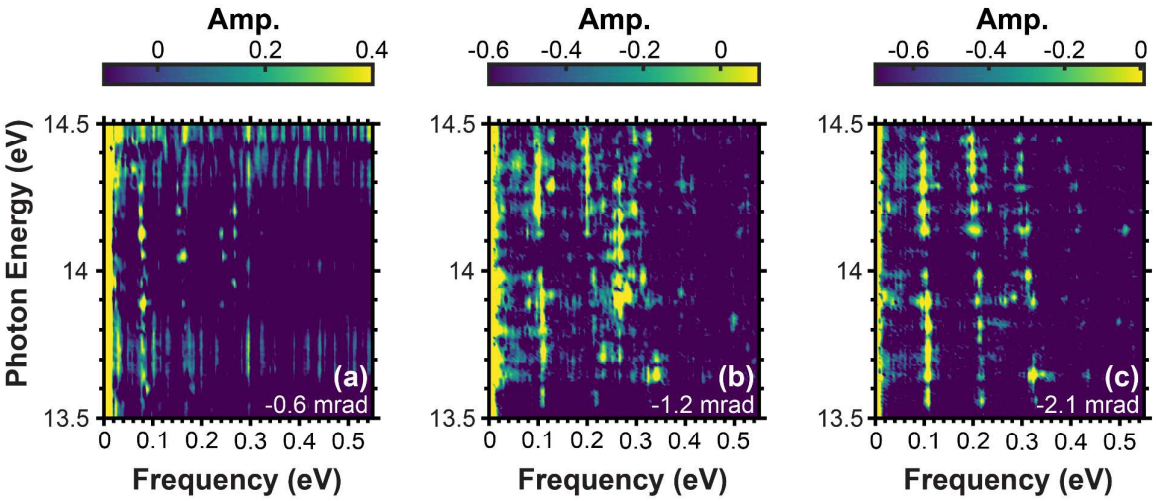

Figure 6: Fourier analysis of time dependent data from Figure 5.

The time evolution of particular absorption and emission features can be examined by integrating over a slice of emission angles. This integration is performed over two pixels, corresponding to an angular spread of 0.258 mrad. Figure 5 shows the delay dependent absorption spectrum of the b′ state features on axis at a divergence angle of -0.65 mrad, and of the emission features found below axis at angles of -1.42 mrad and -2.06 mrad. A Fourier analysis of these spectrograms with respect to the delay axis is presented in Figure 6. The on-axis absorption signals (-0.65 mrad) in Figure 5(a) and Figure 6(a) oscillate at frequencies of 0.077 eV (53.7 fs), 0.160 eV (25.8 fs), and 0.237 eV (17.4 fs). These signals are similar to those reported previously for collinear, single NIR pulse transient absorption experiments.[12,14] Interaction with the copropagating NIR pulse is naturally eliminated in order to satisfy phase matching requirements for the appearance of these features on axis. Therefore, these oscillations result only from the absorption/emission of photons from the XUV beam and the time delayed, angled NIR beam. Previous work has shown that numerous processes can occur in this arrangement, including ac Stark shifts that result in lineshape distortions and Λ/V (lambda/vee) type coupling of bright state levels by the absorption and emission of two photons of NIR light from the delayed pulse.[12,14] For the second process, quantum beats have been observed with frequencies corresponding to the vibrational spacing of the b′ valence state and overtone transitions. The 0.077 eV, 0.160 eV, and 0.237 eV oscillation frequencies observed here are what would be expected from the vibrational spacing of the b′ well: 0.080 eV.[14] The oscillations observed in this experiment are not quite as strong as what has been observed previously, and the overtone transitions are far more limited. This is likely due to the depletion of the original XUV excited b′ wave packet population as a result of the copropagating NIR pulse.

The far below axis emission signals (-2.06 mrad) in Figure 5(c) and Figure 6(c) have a similar pattern of integer multiples of a fundamental frequency, but oscillate at larger frequencies of 0.107 eV (38.6 fs), 0.213 eV (19.4 fs), and 0.315 eV (13.1 fs). These are distinct from what would be observed from the fundamental and overtone transitions of b and b′ bright states of valence character in nitrogen. They also are much smaller than what would be expected for the

fundamental and overtone vibrational frequencies of the inner well of the a″ dark state, which is 0.26 eV. Therefore, we conclude that these oscillations arise from a dark state of valence character that exists around 12 eV, the a″ outer well state. Although it has not previously been observed experimentally, this valence state has been theoretically predicted to have a fundamental vibrational spacing of 0.116 eV and to be considerably anharmonic in shape with a $\omega_e x_e$ value of 0.37 meV.[37] The experimentally measured fundamental vibrational spacing of 0.107 eV is reasonable for a pair of vibrational levels in this well around v=12, corresponding to an energy of 12.4 eV, which is well within our NIR coupling bandwidth with the b′ state. The observed slope in frequencies tends towards lower values for increasing photon energy and non-uniform spacing of the overtone progression in the experimental data also reflects an anharmonic well. There is a 10% change in vibrational frequency over the 1 eV vertical energy range of states in the b′ well exhibiting these quantum beats. This is consistent with theoretical predictions for the $\omega_e x_e$ value of the outer well dark state of 0.37 meV.[37] Further comparison to existing theoretical predictions about the electronic structure of this state[29,31–37] was not possible because this experiment does not provide the exact vibrational level assignment of the participating a″ states.

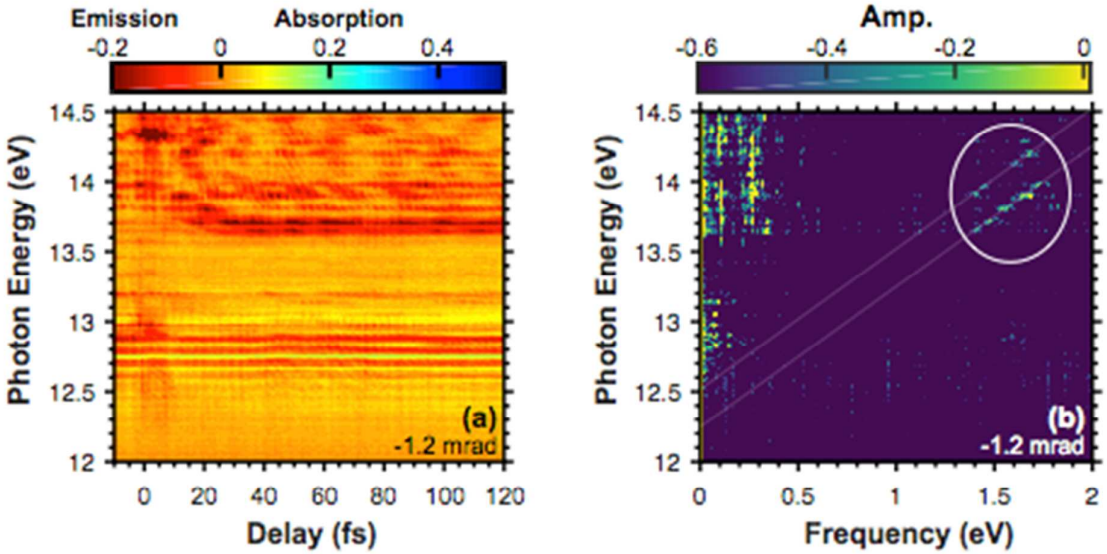

Figure 7: (a) Delay-dependent features for the limited delay range of -10 fs to 120 fs for the intermediate below axis (-1.42 mrad) emission features shown in Figure 5(b). (b) Corresponding Fourier analysis with white circle indicating laser cycle oscillation features. Lines have been overlaid to show the progression of frequencies that allow assignment of dark state energy levels.

The intermediate angle (-1.42 mrad) emission in Figure 5(b) is more complicated, with some of the frequency components found at the other two emission angles, but also an additional strong oscillation at a frequency of 0.267 eV (15.5 fs). These emission features just below axis allow the characterization of the inner a″ well. The pronounced modulation frequency of 0.267 eV matches that expected for the vibrational spacing of the v=0 and v=1 levels of the inner well, 0.265 eV.[39] The oscillations correspond to noncollinear NIR-induced transitions from the two a″ vibrational levels to the same final state, which interfere to cause the quantum beating.

In addition to these modulations in the intermediate (-1.42 mrad) below axis emission features, a regular fast modulation period of approximately 2.6 fs, corresponding to the cycle period of the broad bandwidth NIR pulse, is observed in the states between 13.5 eV and 14.5 eV. Figure 7(a)

presents a limited delay range of -10 fs to 120 fs for this emission angle. In the corresponding Fourier analysis shown in Figure 7(b), these oscillations are revealed to have frequencies between 1.4 eV and 1.9 eV. The Fourier spectrogram is dominated by two linear frequency patterns that correspond to transitions from states at 12.25 eV and 12.52 eV. The higher frequency cycle oscillations come from a slightly different mechanism than the slow modulations discussed above. Similar oscillations have been observed in collinear experiments in atomic systems,[18] and they are ascribed to interferences between a four-wave mixing pathway and the linear absorption pathway. Although this experiment is performed in a noncollinear geometry, the divergence of the harmonics and small crossing angle used in this work allows these two pathways to overlap for the intermediate divergence angles. Because these are transitions from a single dark state to numerous final levels and the frequency of the oscillation is equal to the energy difference between the initial and final states, the frequencies form linear patterns that cross the energy axis at the energetic location of the initial dark state level. In this case, the two patterns correspond to the known a″ inner well dark state levels of 12.254 eV and 12.520 eV.[25,39]

Similar cycle oscillations should be observed from the outer well but are not present in the Fourier analysis. This could be due to the smaller cross section for accessing this state with the original (XUV+NIR) pump or because of the observed larger divergence angles, and therefore reduced interference with the on-axis signal, of the outer well emission features.

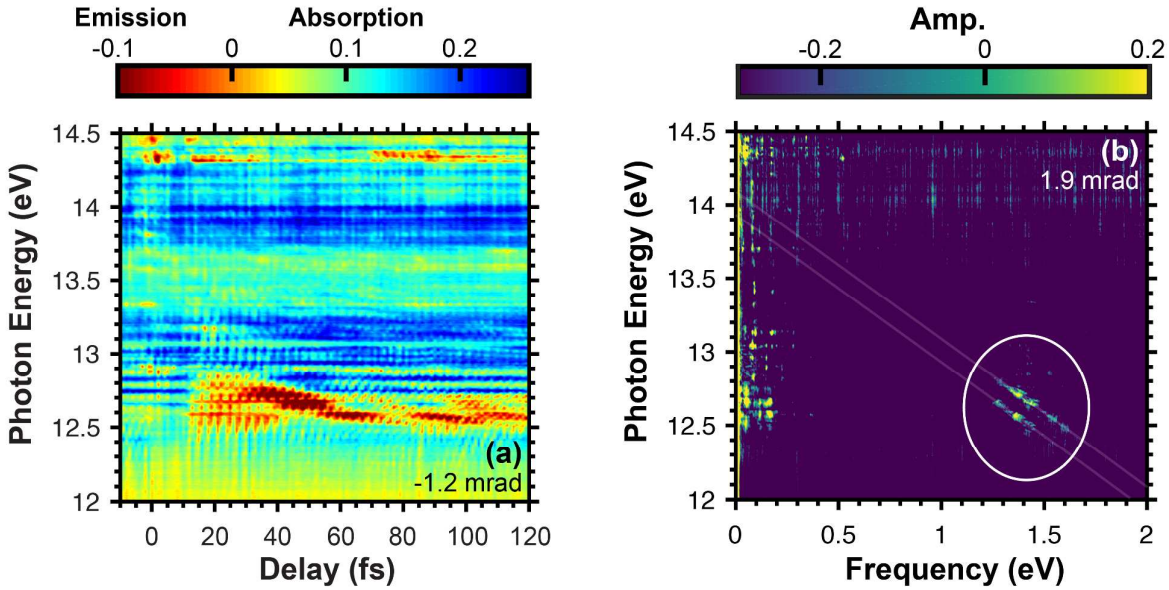

Figure 8: (a) Delay-dependent features for the limited delay range of -20 fs to 280 fs for intermediate above axis (1.93 mrad) emission features. (b) Corresponding Fourier analysis with white circle indicating cycle oscillation features. Lines have been overlaid to show the progression of frequencies that allow assignment of dark state energy levels at 13.932 eV and 14.086 eV belonging to the k and d3 dark Rydberg states.

It is also possible to investigate other dark states using this wave mixing technique. Emission features above the harmonic axis can also be observed at positive divergence angles on the camera image shown in Figure 4(b). The cycle interferences observed in the time-dependence of these features, shown in Figure 8, reveal the location of higher energy dark state levels that are strongly coupled to the lower energy b valence state. Strong contributions from two dark state levels are observed at 13.932 eV and 14.086 eV. The higher energy dark state level has previously been observed in an XUV+NIR REMPI experiment.[27] It can be assigned to the v=0

level of the k dark state, which is the $4d\pi_g$ Rydberg state built on the X N_2^+ ion core. The lower energy level has not been observed before. Recent theoretical calculations[29] and an IR emission experiment[30] suggest a $3d\sigma_g$ Rydberg state built on the X N_2^+ ion core should be located around 13.88 eV. The observed level at 13.932 eV could be the v=0 vibrational level of this d_3 dark state. The observation of interferences in the b state levels, as a result of coupling through these higher energy dark Rydberg states, provides support for lambda and ladder type coupling mechanisms through these dark states, previously assigned to explain the quantum beating in the collinear wave-mixing experiment.[14]

As shown above, using wave-mixing in the noncollinear beam geometry, it is possible to disentangle processes involving different NIR induced pathways. This allows for the creation and observation of dark state wave packets, which can be analysed to reveal the energy level structure of states that are difficult to study using traditional spectroscopies.

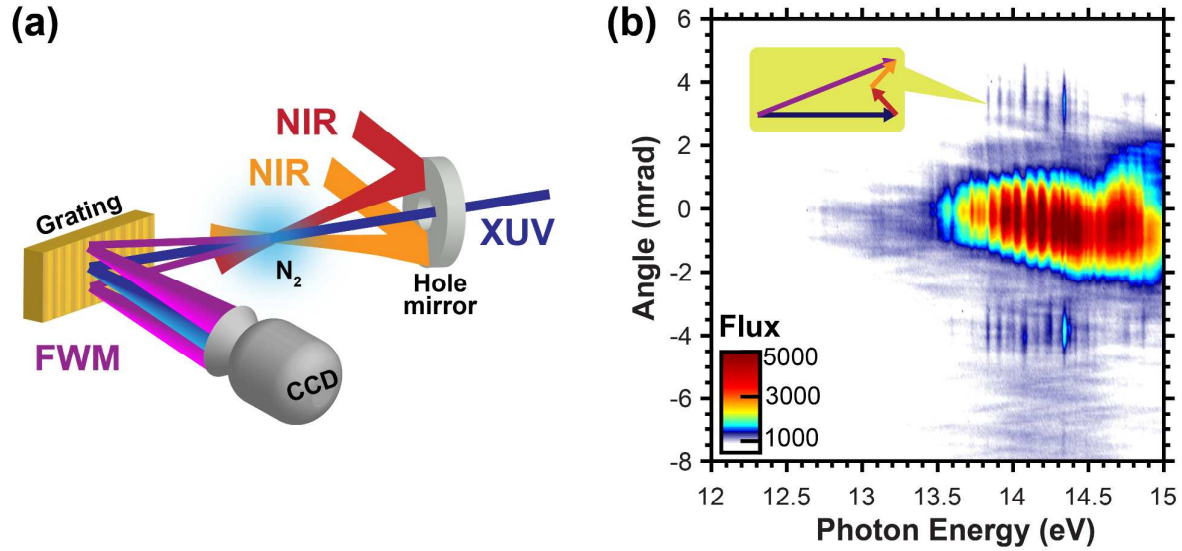

Figure 9: (a) Two NIR and one XUV all-noncollinear experimental geometry and (b) camera image at overlap of XUV+NIR+NIR pulses.

4. Wave packet Control using Two Independently Delayed NIR Pulses – All Three Beams Noncollinear

Experiments using two independently controlled time delays were performed to demonstrate selective wave packet control through the dark a″ state. For these experiments, two independently delayed few-femtosecond NIR pulses interact with the target sample in an XUV + two NIR all-noncollinear geometry as depicted in Figure 9(a). The change in beam interaction geometry was used to implement independent delay control and pulse duration optimization of the two NIR beams. The upper NIR beam is fixed to a constant delay relative to the XUV pulse, while the second, lower NIR beam is introduced at a variable delay. The camera image generated when all three pulses overlap in time is presented in Figure 9(b). The harmonic spectrum used for this experiment, as shown in Figure 9(b) between divergence angles of -2 mrad and 2 mrad, is tuned in order to generate significant flux at 14 eV. It is strongly modulated by absorption features corresponding to the bright states of nitrogen between 13.5 eV and 15 eV. Narrow emission

features are observed off axis both above and below the harmonic beam centered at divergence angles of ±3.5 mrad and energy positions that correspond to dipole allowed states. These emission features can be assigned to specific wave mixing processes based on energy conservation and momentum conservation (phase matching) considerations. Emission features corresponding to a wave-mixing process through the a″ state are found above the harmonic axis in this beam geometry, as shown in the wave-mixing diagram inset in Figure 9(b). With crossing angles of α_1=18 mrad and α_2 = 13 mrad for the two NIR beams relative to the XUV beam, features arising from this process should appear at an angle of $\theta \approx \frac{1.5*\alpha_1+1.5*\alpha_2}{14}$ =3.32 mrad, consistent with the experimental observation of 3.6 mrad.

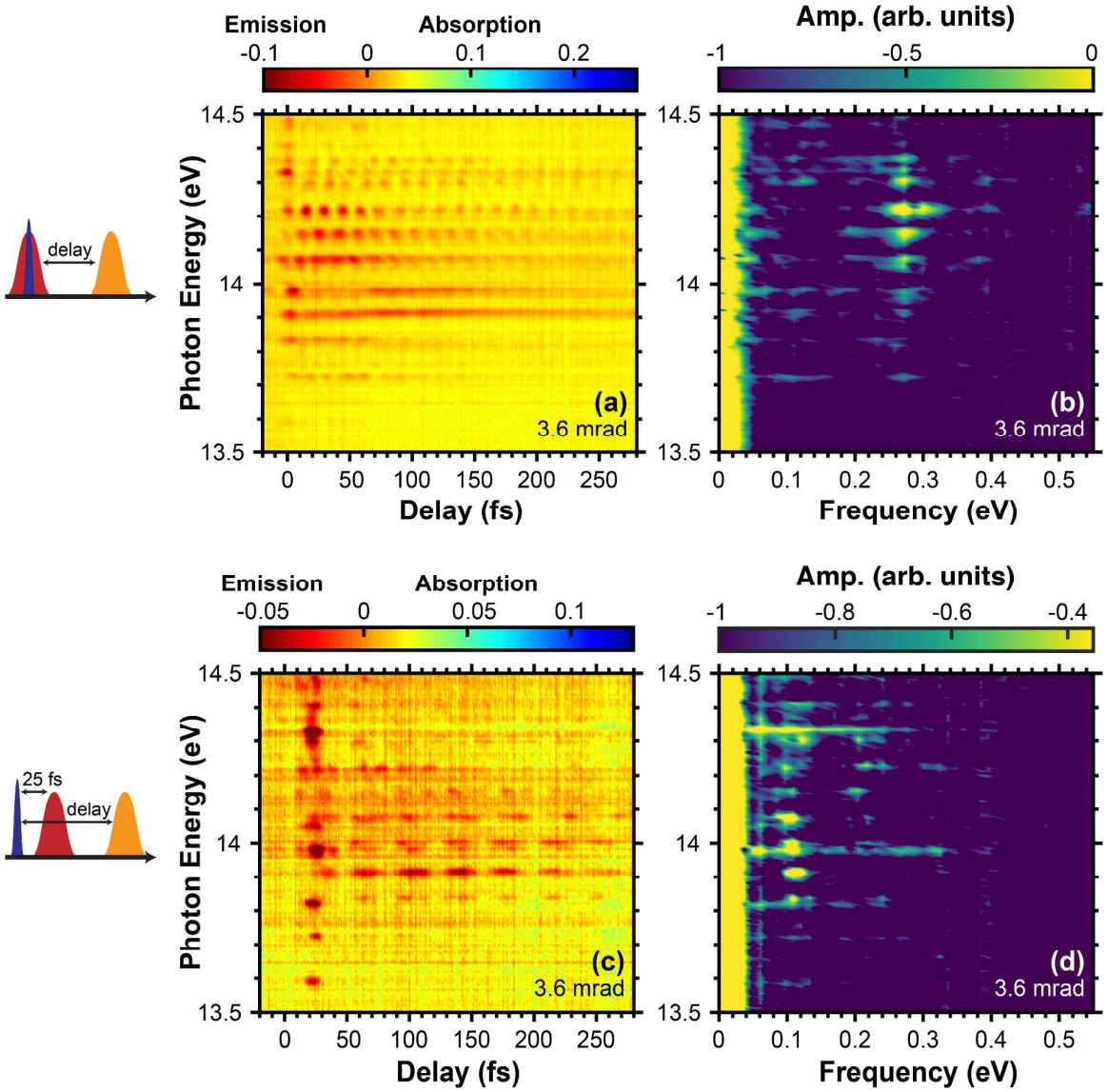

Figure 10: Two NIR and one XUV beam all-noncollinear time-dependent emission. (a) and (b) are the time-dependent absorption and Fourier analysis for data collected with 0 fs delay between the XUV and first NIR pulses. (c) and (d) are the time-dependent absorption and Fourier analysis for data collected with a 25 fs fixed delay between the XUV and first NIR pulses. The time delay axis in (a) and (c) is the delay between the XUV pulse and the second, scanned, NIR pulse.

Two different pulse sequences are used in this all-noncollinear geometry. In the first, one NIR pulse is fixed at a delay of 0 fs relative to the exciting XUV pulse while the second NIR pulse is scanned. In the second pulse sequence, the time delay between the XUV and one of the NIR pulses is fixed at 25 fs, while the second NIR pulse is scanned with delays relative to the first NIR pulse. With these pulse sequences, only emission features where the last photon for the wave mixing process comes from the second, variably delayed NIR pulse will show non-trivial time dependence that persists after overlap of all three pulses. In this beam geometry, these are the emission features found at positive emission angles. In Figure 10(a) and (c), the delay dependence of these emission features is presented after integrating over the 3.6 mrad emission features for the 0 fs and 25 fs delay conditions, respectively. A Fourier analysis of each spectrogram is presented in Figure 10(b) and (d) in order to determine the periods of the intensity oscillations for each bright state feature. For the 0 fs time delay pulse sequence analyzed in Figure 10(b), a common oscillation frequency of 0.267 eV is observed for the features between 13.9 eV and 14.4 eV. Emission features below 14 eV show substantially weaker oscillations at this same frequency or no oscillations at all. In the analysis performed for the 25 fs time delay pulse sequence presented in Figure 10(d), a much lower frequency oscillation is observed around 0.1 eV. These signals are strongest for energies between 13.8 eV and 14.3 eV. The oscillation frequencies characterize the wave packet produced and probed in the a″ dark state on the inner and outer turning points for the 0 fs and 25 fs delay cases, respectively, discussed next.

Emission will be observed as a result of four-wave mixing, with amplitudes determined by the strength of the XUV and NIR coupling processes. Oscillations in emission intensity with time delay, as is observed for the features in Figure 10, occur as a result of multiple four-wave mixing processes that end up in the same final detector state level. For these experiments, where the time delay of the NIR pulse that couples the dark state levels to the final bright state levels is scanned, these absorption oscillations must be due to mixing processes that involve distinct dark state levels. Given that the phase matching constraints require the dark state that is accessed be lower than 14 eV in energy, and the known bandwidth of the NIR pulse is centred around 1.75 eV, the dark state being probed in this experiment is the a″ state, which has known vibrational levels between 12 eV and 13 eV. For the spectrogram collected with the first NIR pulse at 0 fs delay, the observed oscillation frequency of 0.267 eV is precisely what is predicted from the known vibrational spacing of 0.266 eV for the v=0 and v=1 levels of the a″ Rydberg-like, inner well dark state. With this pulse sequence, the initially excited bright state wave packet in the b′ state is created in the ground state Franck-Condon region. The vibrational wave packet that is excited in the b′ state remains localized at 0 fs while the first NIR pulse projects its population to the a″ state. The inner well a″ Rydberg state is similar in bond length to the ground state of nitrogen, so the vibrational overlap between it and the b′ wave packet is excellent for these early times. Thus, the 0 fs delay NIR pulse projects the b′ wave packet primarily into the inner well dark state, populating the lowest two vibrational levels with some intensity. With this pulse sequence, no outer well dark state is observed within the experimental signal-to-noise ratio. This is consistent with a treatment of the inner and outer potential wells as non-interacting for the levels that can be accessed with the few-femtosecond NIR pulses.[33,34]

The situation changes when the delay of the first NIR pulse is adjusted to 25 fs, as is illustrated in the cartoon shown in Figure 2. Using a delay of 25 fs, which is half the vibrational period of the b′ state, the vibrational wave packet originally excited by the XUV pulse has time to reach its outer turning point before the NIR pulse projects the population down to a dark state. At these extended bond lengths, the Frank-Condon overlap with the a″ inner well is negligible. This explains the absence of an experimentally detectable 0.266 eV oscillation frequency in Figure 10(d) for the emission features generated with this pulse sequence. The valence-like outer well a″ dark state is predicted to have considerably extended bond lengths as well, and the Franck-Condon overlap with this state should dominate for this pulse sequence. This is exactly what is observed, with the measured oscillation frequency of 0.1 eV closely matching the theoretically calculated value expected for this state and the fundamental frequency quantum beats that were observed in the noncollinear experimental geometry.

This experiment demonstrates wave packet control in the XUV using a multidimensional transient wave-mixing technique. The fine control of time evolution in an excited state potential energy surface achieved using multiple ultrafast preparation pulses allows selective preparation and probing of a non-Franck Condon region of the potential energy surface of nitrogen. Although only a bound, neutral species is studied in this experiment, it is similar in concept to the Tannor-Kosloff-Rice control scheme, where time evolution in an excited potential energy surface is used to control the creation of desired photoproducts.[43] Conventional control schemes to study molecular potential surfaces have also relied on the detection of ionization processes with the control parameters of iterative pulse shape optimization[44,45] or R-dependent ionization,[46] requiring considerable theoretical support and foreknowledge of the electronic structure of system being studied for interpretation. In contrast, the exceptional time, spectral, and angular resolution offered by transient wave-mixing allows for the isolation and control of particular pathways of interest in neutral species, providing a direct probe of the specific wavepacket dynamics of interest.

5. Conclusion

Transient four wave mixing spectroscopy is used to investigate the electronic structure of a dark state of molecular nitrogen in the XUV spectroscopically and dynamically. Two photon excitation is used to prepare a wave packet in the a″ state. This wave packet is probed by a few-femtosecond noncollinear NIR pulse, which creates background-free emission signals. The spatial location of these signals allows for the assignment of the dark state energy levels to lambda or vee type coupling pathways. The broad bandwidth of the NIR pulse can couple multiple dark state levels to the same final bright state detector level, leading to the observation of quantum beats when the delayed NIR pulse is scanned in time. The frequencies of the observed quantum beats correspond to the energy level structure of the dark electronic states, allowing for the measurement of their vibrational and electronic properties. A double well potential formed by an avoided crossing was characterized using this nonlinear technique, which probed below the crossing point to study a Rydberg-like state with small internuclear bond distances and widely separated vibrational levels and a valence state with extended bond lengths and closely spaced vibrational levels.

Building upon these observations, a truly multidimensional XUV experiment was performed by adding an additional time delay between the XUV and first NIR pulse. This delay was chosen such that either the inner or outer turning point of the wave packet created by the XUV pulse in the b′ state was coupled to the a″ dark state. Due to the different internuclear distances of the Rydberg and valence dark state wells, this allows for the selective population of these dark states. This wave packet control was confirmed by the observed quantum beats in the emission signal created by the second, variable time delayed NIR pulse. The ability of this multidimensional technique to selectively control wave packets and probe non-Franck-Condon regions of molecular potential surfaces highlights its potential application to the molecular spectroscopy of more complex systems, which have been difficult to study with standard linear absorption techniques. Future experiments will extend XUV wave mixing to explore molecular dynamics using the first interpulse delay to monitor the dephasing of the bright state wave packet or the decay of specific excited states. In addition, the superb energy, time, and angular resolution of this technique can be used to completely reconstruct wave packet motion for a reactive species, a longstanding goal of time-resolved spectroscopies.[47]

Conflict of interest

There are no conflicts of interest to declare.

Acknowledgements

This work was supported by the Director, Office of Science, Office of Basic Energy Sciences and by the Division of Chemical Sciences, Geosciences, and Biosciences of the U.S. Department of Energy at LBNL under Contract No. DE-AC02-05CH11231. APF acknowledges funding from the NSF Graduate Research Fellowship Program.

References

1 J. R. Andrews, R. M. Hochstrasser and H. P. Trommsdorff, *Chem. Phys.*, 1981, **62**, 87–101.
2 K. W. Stone, K. Gundogdu, D. B. Turner, X. Li, S. T. Cundiff and K. A. Nelson, *Science*, 2009, **324**, 1169–1174.
3 O. Golonzka, M. Khalil, N. Demirdoven and A. Tokmakoff, *Phys. Rev. Lett.*, 2001, **86**, 2154–2157.
4 A. Halpin, P. J. M. Johnson, R. Tempelaar, R. S. Murphy, J. Knoester, T. L. C. Jansen and R. J. D. Miller, *Nat. Chem.*, 2014, **6**, 196–201.
5 N. A. Kurnit, I. D. Abella and S. R. Hartmann, *Phys. Rev. Lett.*, 1964, **13**, 567–568.
6 M. Schmitt, G. Knopp, A. Materny and W. Kiefer, *Chem. Phys. Lett.*, 1997, **270**, 9–15.
7 E. J. Brown, Q. G. Zhang and M. Dantus, *J. Chem. Phys.*, 1999, **110**, 5772–5788.
8 P. Hamm and M. T. Zanni, *Concepts and Methods of 2D Infrared Spectrocopy*, Cambridge University Press, 2011.
9 R. L. Swofford and A. C. Albrecht, *Annu. Rev. Phys. Chem.*, 1978, **29**, 421–440.
10 S. Mukamel, D. Healion, Y. Zhang and J. D. Biggs, *Annu. Rev. Phys. Chem.*, 2013, **64**, 101–127.
11 S. R. Leone and D. M. Neumark, *Faraday Discuss.*, 2016, **194**, 15–39.
12 E. R. Warrick, W. Cao, D. M. Neumark and S. R. Leone, *J. Phys. Chem. A*, 2016, **120**, 3165–3174.
13 M. Reduzzi, W. Chu, C. Feng, A. Dubrouil, J. Hummert, F. Calegari, F. Frassetto, L. Poletto, O. Kornilov, M. Nisoli, C.-D. Lin and G. Sansone, *J. Phys. B*, 2016, **49**, 65102.
14 E. R. Warrick, J. E. Bækhøj, W. Cao, A. P. Fidler, F. Jensen, L. B. Madsen, S. R. Leone and D. M. Neumark, *Chem. Phys. Lett.*, 2017, 683, 408–415.
15 Y. Cheng, M. Chini, X. Wang, A. González-Castrillo, A. Palacios, L. Argenti, F. Martín and Z. Chang, *Phys. Rev. A*, 2016, **94**, 23403.
16 W. Cao, E. R. Warrick, A. Fidler, D. M. Neumark and S. R. Leone, *Phys. Rev. A*, 2016, **94**, 53846.
17 W. Cao, E. R. Warrick, A. Fidler, S. R. Leone and D. M. Neumark, *Phys. Rev. A*, 2018, **97**, 23401.
18 T. Ding, C. Ott, A. Kaldun, A. Blättermann, K. Meyer, V. Stooß, M. Rebholz, P. Birk, M. Hartmann, A. Brown, H. Van, D. Hart, T. Pfeifer, V. Stooss, M. Rebholz, P. Birk, M. Hartmann, A. Brown, H. Van Der Hart and T. Pfeifer, *Opt. Lett.*, 2016, **41**, 709.
19 P. K. Carroll and C. P. Collins, *Can. J. Phys.*, 1969, **47**, 563–589.
20 H. Lefebvre-Brion, *Can. J. Phys.*, 1969, **47**, 541–545.
21 K. Dressler, *Can. J. Phys.*, 1969, **47**, 547–561.

22 A. J. Yencha, K. Ellis and G. C. King, *J. Electron Spectros. Relat. Phenomena*, 2014, **195**, 160–173.
23 K. P. Huber and C. Jungen, *J. Chem. Phys.*, 1990, **92**, 850.
24 K. R. Lykke and B. D. Kay, *J. Chem. Phys.*, 1991, **95**, 2252–2258.
25 T. F. Hanisco and A. C. Kummel, *J. Phys. Chem.*, 1991, **95**, 8565–8574.
26 M. J. J. Vrakking, A. S. Bracker and Y. T. Lee, *J. Chem. Phys.*, 1992, **96**, 7195–7196.
27 A. de Lange and W. Ubachs, *Chem. Phys. Lett.*, 1999, **310**, 471–476.
28 A. de Lange, R. Lang, W. van der Zande and W. Ubachs, *J. Chem. Phys.*, 2002, **116**, 7893.
29 D. A. Little and J. Tennyson, *J. Phys. B*, 2014, **47**, 105204.
30 D. Cossart and C. Cossart-Magos, *J. Chem. Phys.*, 2004, **121**, 7148–7152.
31 H. H. Michels, *J. Chem. Phys.*, 1970, **53**, 841–2.
32 H. H. Michels, *Adv. Chem. Phys.*, 1981, **445**, 225–340.
33 W. C. Ermler, A. D. McLean and R. S. Mulliken, *J. Phys. Chem.*, 1982, **86**, 1305–1314.
34 W. C. Ermler, J. P. Clark and R. S. Mulliken, *J. Chem. Phys.*, 1987, **86**, 370.
35 S. L. Guberman, *J. Phys. Chem. A*, 2007, **111**, 11254–11260.
36 M. Hochlaf, H. Ndome, D. Hammoutène and M. Vervloet, *J. Phys. B*, 2010, **43**, 245101.
37 S. L. Guberman, *J. Chem. Phys.*, 2012, **137**, 74309.
38 J. Bominaar, C. Schoemaecker, N. Dam, J. J. Ter Meulen and G. C. Groenenboom, *Chem. Phys. Lett.*, 2007, **435**, 242–246.
39 E. J. Salumbides, A. Khramov and W. Ubachs, *J. Phys. Chem. A*, 2009, **113**, 2383–2386.
40 P. K. Carroll and K. V. Subbaram, *Can. J. Phys.*, 1975, **53**, 2198–2209.
41 A. W. Kam and F. M. Pipkin, *Phys. Rev. A*, 1991, **43**, 3279–3284.
42 H. Mashiko, S. Gilbertson, C. Li, S. D. Khan, M. M. Shakya, E. Moon and Z. Chang, *Phys. Rev. Lett.*, 2008, **100**, 103906.
43 D. J. Tannor, R. Kosloff and S. A. Rice, *J. Chem. Phys.*, 1986, **85**, 5805–5820.
44 B. Schafer-Bung, R. Mitric, V. Bonacic-Koutecky, A. Bartelt, C. Lupulescu, A. Lindinger, S. Vajda, S. M. Weber and L. Woste, *J. Phys. Chem. A*, 2004, **108**, 4175–4179.
45 T. Frohnmeyer and T. Baumert, *Appl. Phys. B*, 2000, **71**, 259–266.
46 M. Wollenhaupt, A. Assion, O. Graefe, D. Liese, C. Sarpe-Tudoran, M. Winter and T. Baumert, *Chem. Phys. Lett.*, 2003, **376**, 457–464.
47 D. Avisar and D. J. Tannor, *Phys. Rev. Lett.*, 2011, **106**, 1–4.